

# Quantitative *in vivo* measurements of blood oxygen saturation using multiwavelength photoacoustic imaging

J. Laufer<sup>†</sup>, E. Zhang, P. Beard

Department of Medical Physics & Bioengineering, University College London,  
Malet Place Engineering Building, London WC1E 6BT, UK,

<http://www.medphys.ucl.ac.uk/research/mle/index.htm>

## ABSTRACT

Multiwavelength photoacoustic imaging was used to make spatially resolved measurements of blood oxygen saturation ( $sO_2$ ) *in vivo*. 2D cross-sectional images of the initial absorbed optical energy distribution in the finger were acquired at near-infrared wavelengths using a photoacoustic imaging system. Using the structural information from these images, a 2D finite element forward model of the light transport was formulated to calculate the absorbed energy density in the tissue as a function of the concentrations of the tissue chromophores and scatters. Separate oxy- ( $HbO_2$ ) and deoxyhaemoglobin (HHb) concentrations were assigned to locations within the mesh that corresponded to the locations of blood vessels in the detected photoacoustic image. The surrounding tissue was regarded as a homogeneous medium with optical properties that were determined by the concentrations of water, lipids, optical scatters, and  $HbO_2$  and HHb in the capillary bed. The concentrations of the individual chromophores were the variable input parameters of the forward model. By varying their values in a minimisation procedure in order to fit the output of the model to the measured multiwavelength images, the  $HbO_2$  and HHb concentrations, and hence blood  $sO_2$ , within the blood vessels were determined.

## 1. INTRODUCTION

Photoacoustic spectroscopy offers the potential to provide spatially resolved quantitative physiological and molecular information by exploiting the known spectral characteristics of specific chromophores. For example, by obtaining images at multiple wavelengths it is, in principle, possible to quantify the local concentrations of spectrally distinct endogenous chromophores such as oxyhaemoglobin ( $HbO_2$ ) and deoxyhaemoglobin (HHb) for the calculation of absolute blood oxygen saturation ( $sO_2$ ).

Recent efforts to make such measurements have acknowledged the limitations in assuming that the absorbed optical energy at a specific point is linearly dependent on the absorption spectra of the chromophores at that point [1-3]. The wavelength dependent absorption and scattering in the space surrounding a specific point will affect the detected absorbed energy spectrum, which compromises the use of simple linear spectral decomposition techniques such as those used in conventional optical spectroscopy. To overcome these limitations, different approaches have been suggested in order to obtain empirical correction factors. These have included measuring the spectral attenuation of the tissue overlaying the region of interest using excised tissue [3] or measuring the photoacoustic spectrum of an absorber of known absorption spectrum inserted beneath the skin at the depth of interest [1]. However, apart from the invasive nature of obtaining such correction factors, their main drawback is the lack of generality as they are strongly dependent upon, for example, tissue type, composition and blood perfusion.

A fundamentally different approach has recently been shown to allow the spatially resolved and quantitative determination of chromophore concentrations from photoacoustic waveforms detected at a single point in a realistic tissue phantom [4]. This study concluded that a model of the light transport, which calculates the absorbed optical energy distribution as a function of wavelength together with a model of the acoustic propagation are essential in order to extract quantitative information from wavelength-dependent photoacoustic signals. In the light transport model, the spatial distribution of  $\mu_a$  was expressed in terms of the local chromophore concentrations. By fitting the modelled

---

<sup>†</sup> Correspondence email: [jlaufer@medphys.ucl.ac.uk](mailto:jlaufer@medphys.ucl.ac.uk)

wavelength-dependent photoacoustic signals to the detected waveforms, the absolute concentrations of all chromophores and derived parameters, such as blood sO<sub>2</sub>, were determined.

This study aims to extend this method to the analysis of 2D (and eventually 3D) photoacoustic images. Ultimately, quantitative photoacoustic imaging requires a generally applicable method in which a forward model of the absorbed energy distribution is fitted to the detected photoacoustic images by varying the concentrations of chromophores and scatterers for each image pixel independently until convergence is achieved. Such a methodology offers the prospect of providing quantitative three-dimensional maps of HbO<sub>2</sub> and HHb concentrations and blood sO<sub>2</sub>. It could also be used to identify and quantify the accumulation of externally administered contrast agents such as those used in molecular imaging applications [5,6]. A first step towards this goal is described in this paper. A study was conducted in which multiwavelength photoacoustic images of a tissue phantom, which comprised a scattering liquid and dye-filled tubes, were analysed using a forward model of the absorbed energy density in order to recover the absolute concentrations of the dyes. This was followed by a preliminary *in vivo* study in which images of a human finger were analysed to determine the HbO<sub>2</sub> and HHb concentrations, and hence blood sO<sub>2</sub>, in the blood vessels and the extravascular space, i.e. the capillary bed.

## 2. BACKGROUND

### 2.1. Model-based inversion

This section describes the model-based inversion scheme for recovering the absolute concentrations of specific chromophores from a set of measured multiwavelength photoacoustic images. This requires that a mathematical forward model is formulated to describe the physical processes involved in the generation of these images. The model is then inverted to recover the absolute values of the chromophore concentrations from the measured data.

An image of the distribution of the absorbed optical energy density in the target is reconstructed from detected photoacoustic signals by using an acoustic backprojection algorithm. By acquiring images at different wavelengths, absorbed energy spectra can thus be obtained for each point in the image. However, these spectra are not simply proportional to the combined absorption by the local chromophores. Instead, they are the product of the local absorption coefficient and the fluence, the latter being a function of the spatial distribution of the spectral absorption and scattering characteristics of all the chromophores and scatterers within the illuminated volume. In order to reconstruct the spatial distribution of the absorption coefficient, and hence the local chromophore concentrations, from these images, it is necessary to use a mathematical model of light transport that is capable of calculating images of the absorbed optical energy density for arbitrary chromophore distributions. The model is inverted by varying the chromophore concentrations until the difference between the detected and predicted images is minimised. The values that produced the smallest difference were regarded as those most likely to be the true values. The inversion required *a priori* the specific absorption coefficient spectra of the chromophores and the wavelength dependence of the scattering coefficient.

#### 2.1.1. The forward model

The forward model was a diffusion-based 2D finite element model (FEM). This was used to calculate the initial absorbed energy distribution,  $Q$ . The FEM incorporated the delta-Eddington approximation to improve the accuracy in  $Q$  close to the source [7]. The calculated absorbed energy density can be described as

$$Q(x, z, \mu_a(x, z), \mu_s, g) = \mu_a(x, z) \Phi_0 \Phi(x, z, \mu_a(x, z), \mu_s, g) \quad (1)$$

where  $x$  is the horizontal distance and  $z$  the vertical distance from the illuminated surface.  $\Phi$  is the internal fluence distribution normalised to that at the surface,  $\Phi_0$ , and  $g$  is the scattering anisotropy factor.

The model is used in the following manner. Firstly, although the FE model is general in the sense that it can account for arbitrary distributions of optical coefficients, its current implementation requires that the target geometry is recovered from the measured absorbed energy images and incorporated directly in the model. Thus in the case of one of the tissue phantoms studied in this paper, which comprised three dye filled tubes immersed in a homogenous scattering liquid, the FE grid is set up to represent three absorbers in a uniform scattering background. This is illustrated in Figure 1, which shows the output of the forward model for this configuration. The unknown parameters are the absorption coefficients of the absorbers,  $\mu_{ai}$ , and the absorption and scattering coefficients of the background,  $\mu_{ae}$  and  $\mu_s$ ,

respectively. The FEM was formulated similarly for the analysis of the *in vivo* images, where the absorbing regions in the model represented the blood vessels.

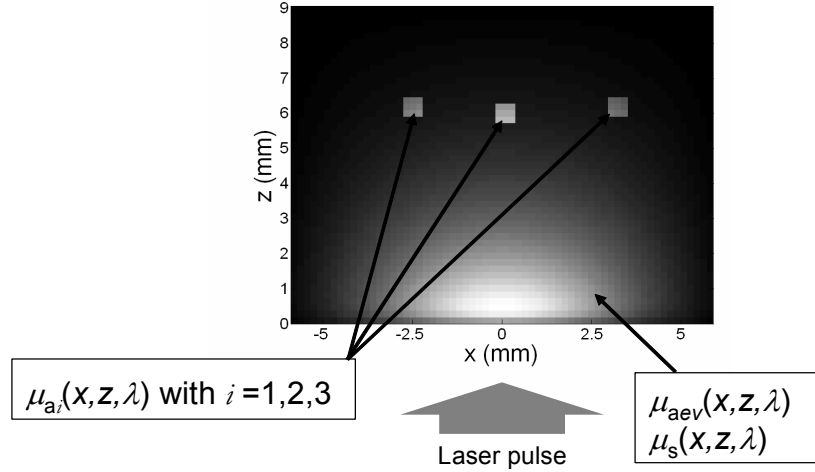


**Figure 1** An example of the output of the model for a phantom comprising three dye-filled tubes immersed in a homogeneous scattering medium. The location of the tubes (or blood vessels for *in vivo* measurements) as well as the profile and position of the excitation beam were obtained from the detected photoacoustic images, an example of which is shown in Figure 3.

The wavelength-dependent absorption coefficient is defined in terms of chromophore concentrations as

$$\mu_a(\lambda) = \sum \alpha_j(\lambda) c_j \quad (2)$$

where  $\alpha_j(\lambda)$  is the known specific absorption coefficient of chromophore  $j$  while  $c_j$  is its concentration. For the tissue phantom experiments, the absorption coefficients of the absorbing regions ( $\mu_{ai}(\lambda)$  in Figure 1) were defined using equation (2) in terms of the concentrations and specific absorption coefficients of the dyes used, while the absorption coefficient of the medium surrounding the tubes,  $\mu_{aev}(\lambda)$ , was that of water. For the *in vivo* experiments,  $\mu_{ai}(\lambda)$  was defined using equation (2) in terms of intravascular HbO<sub>2</sub> and HHb concentrations, while  $\mu_{aev}(\lambda)$  was expressed in terms of water absorption and the extravascular HbO<sub>2</sub> and HHb concentrations to account for the blood absorption in the capillary bed. The scattering coefficient,  $\mu_s$ , within the target was assumed to be homogeneously distributed over the domain but variable in value and was expressed as

$$\mu_s(\lambda) = \alpha_{\text{scat}}(\lambda) k_{\text{scat}} \quad (3)$$

where  $\alpha_{\text{scat}}(\lambda)$  is the wavelength-dependent scattering efficiency and  $k_{\text{scat}}$  is a scaling factor.  $\alpha_{\text{scat}}(\lambda)$  was obtained from  $\mu_s$  spectra measured in Intralipid [8]. The scattering anisotropy factor,  $g$ , was assumed independent of wavelength and set to 0.9.

The forward model was inverted by varying the adjustable unknown input parameters (i.e.  $c_j$ ,  $k_{\text{scat}}$ , and  $\Phi_0$ ) iteratively until the difference between the measured and modelled images was minimised. Having obtained the concentrations of oxy- and deoxyhaemoglobin from the *in vivo* measurements, the blood sO<sub>2</sub> was calculated for each blood vessel using

$$\text{sO}_2 = \frac{c_{\text{HbO}_2}}{c_{\text{HHb}} + c_{\text{HbO}_2}} \times 100\% . \quad (4)$$

For the tissue phantom experiments, a chromophore concentration ratio,  $R_{\text{dye}}$ , was calculated as an analogue to blood sO<sub>2</sub>, from the determined concentrations of two dyes.  $R_{\text{dye}}$  was defined as

$$R_{\text{dye}} = \frac{c_1}{c_1 + c_2} \times 100\% . \quad (5)$$

### 3. METHODS

In order to test the proposed method on a structurally simple but optically and acoustically well-controlled target, a tissue phantom was constructed. The aim of the tissue phantom study was to answer a) whether the method is able to detect the presence of specific chromophores, b) how accurately it can determine the ratio of chromophore concentrations (i.e. perform blood  $sO_2$ -type measurements) and, ultimately, c) how accurately it can quantify absolute concentrations.

#### 3.1. 2D forward mode imaging of tissue phantom

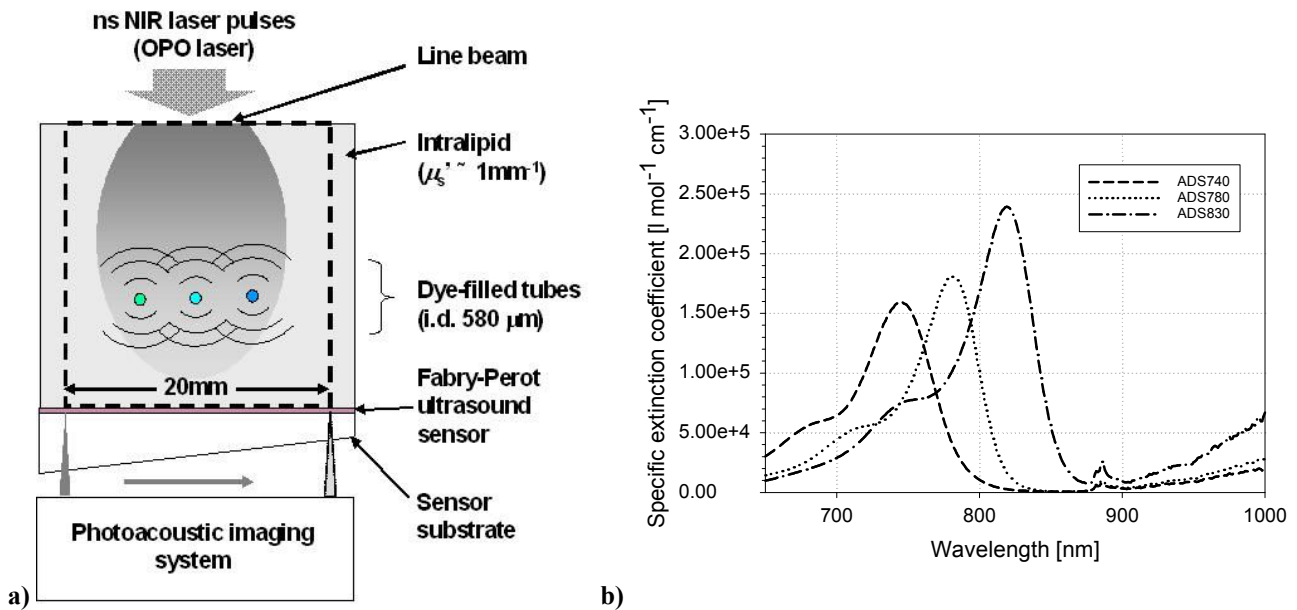


**Figure 2** a) The tissue phantom consisted of a bath of diluted Intralipid in which up to three dye-filled tubes were submerged at a depth of approximately 6.5mm. The generated photoacoustic waves were detected at 400 points along a 20mm line scan. (b) The specific absorption spectra of the near-infrared dyes.

Figure 2(a) shows the tissue phantom, which consisted of up to three tubes that were immersed in Intralipid diluted to produce  $\mu_s' \sim 1.3\text{mm}^{-1}$ . The tubes were filled with mixtures made from three near-infrared dyes (American Dye Source) dissolved in methanol, the absorption spectra of which are shown in Figure 2(b). Combinations of two of dyes were mixed at different concentration ratios in order to produce qualitative changes in the absorption spectrum that are analogous to those produced by different ratios of  $c_{HbO_2}$  and  $c_{Hb}$  in blood. The phantom was illuminated with nanosecond laser pulses from an OPO laser system at 15 wavelengths between 740nm and 990nm. An elliptical beam ( $4\text{mm} \times 25\text{mm}$ ) was used to approximate the 2D source geometry of the FEM described in section 2.1.1. The fluence at the surface was  $<35\text{mJ cm}^{-2}$ . The generated photoacoustic waves were detected using a photoacoustic imaging system, which is described in detail in [9]. Its ultrasound sensing mechanism is based on the interferometric detection of acoustically induced changes in the optical thickness of a Fabry-Perot interferometer, which is formed by a polymer film sandwiched between two dielectric mirrors. A line scan was performed to record one photoacoustic signal every 0.05mm over a 20mm line. From this data, photoacoustic images of the absorbed energy density were obtained using a 2D Fourier transform image reconstruction algorithm [10]. An example of a typical image is shown in Figure 3.

Two sets of measurements were performed: a) in phantoms with a single tube, which provided a simple geometry to test the method, and b) in phantoms with three tubes to test a more complex structure. The latter experiments proved useful in assessing the accuracy of the method at retrieving absolute concentrations when compromised by errors such as the position of the tubes relative to the incident beam.

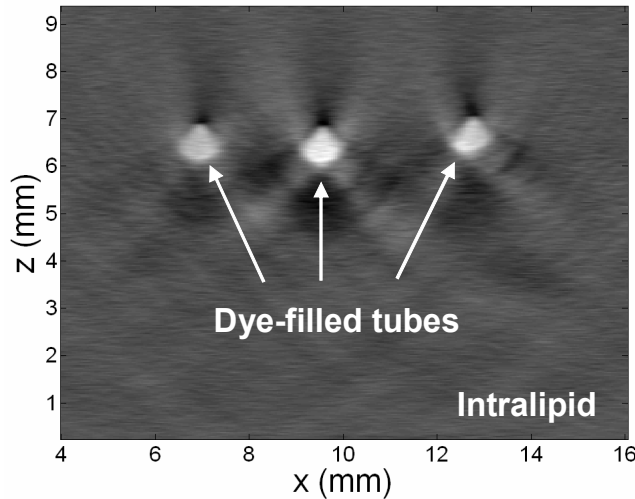


**Figure 3** A typical photoacoustic image obtained in a tissue phantom comprising three dye-filled tubes immersed in Intralipid at 801nm. The information contained in such images was used to specify the location of absorbing regions in the FEM as described in section 2.1.1.

### 3.2. *In vivo* 2D backward mode imaging

The middle finger was submerged in a water bath to provide the acoustic coupling to the sensor head of the photoacoustic imaging system. The imaging system was used in backward mode, that is to say the excitation laser pulses were directed through the optically transparent Fabry-Perot ultrasound detector so that the photoacoustic signals are detected on the same side of the tissue that the laser pulses are directed to. The excitation beam was circular and had a diameter of 1.5cm at the sensor surface, which resulted in a maximum fluence of  $17\text{mJ cm}^{-2}$ . A 20mm line scan (0.05mm increments) of the middle section of a finger was carried out at excitation wavelengths between 740nm and 980nm at increments of 20nm.

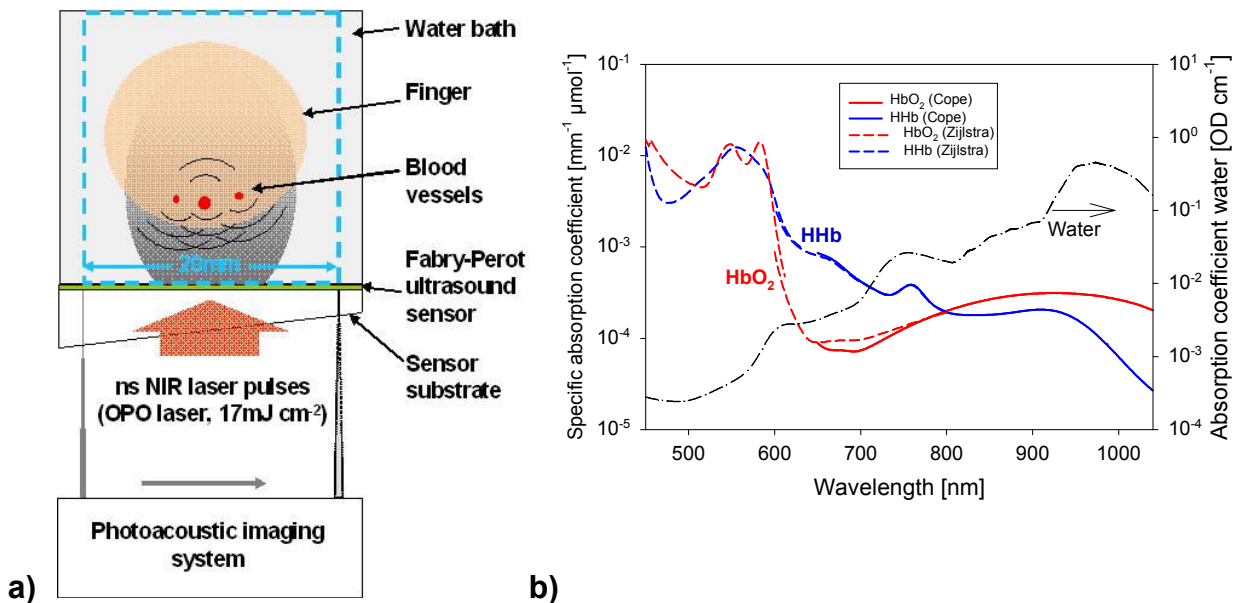


**Figure 4** a) Photoacoustic waves were generated in the middle finger, which was illuminated by ns laser pulses from the OPO laser. The laser pulses were transmitted through the Fabry-Perot ultrasound sensor (backward mode). b) The specific absorption spectra of the main tissue chromophores oxy- and deoxyhaemoglobin and water in the near-infrared wavelength region.

A typical photoacoustic image of the finger is shown in Figure 5, which shows the epidermis and distinct blood vessels underneath the dermis. The blood vessels are located at a depth of 1 to 2mm. The blood vessels marked 1 to 3 were analysed to determine the intravascular oxy- and deoxyhaemoglobin concentrations,  $c_{\text{HbO}_2}$  and  $c_{\text{HHb}}$ , from which the total haemoglobin concentration,  $c_{\text{THb}}=c_{\text{HbO}_2}+c_{\text{HHb}}$ , and the blood  $\text{sO}_2$  were calculated. The location of the absorbing regions within the FEM grid (section 2.1.1) was again based on the detected image. For this model inversion, the scattering coefficient was kept at a fixed value of  $\mu_s=12\text{mm}^{-1}$ .

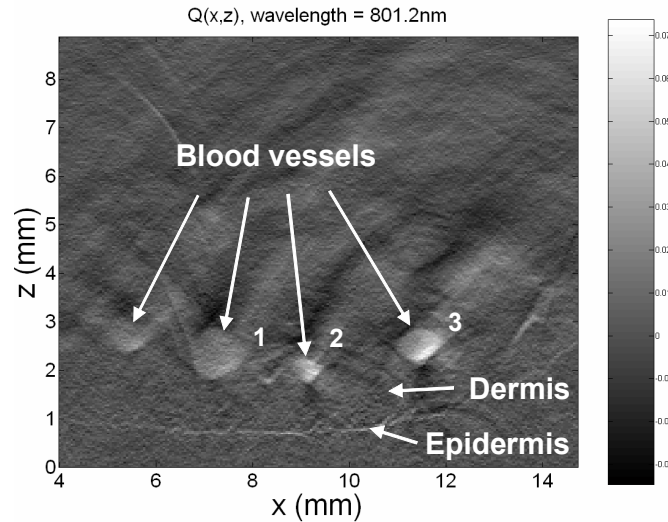


**Figure 5** Photoacoustic image of the back of a finger detected at 801.2nm. The image shows the outline of the skin (epidermis) and the blood vessels located beneath the dermis at a depth of 1 to 1.5mm. The blood vessels marked 1 to 3 were analysed to determine the  $\text{HbO}_2$  and  $\text{HHb}$  concentrations and blood  $\text{sO}_2$ .

## 4. RESULTS

### 4.1. Tissue phantom results

Table 1 shows the known and photoacoustically determined dye concentrations,  $\text{PA } c_{\text{dye}}$ , the derived chromophore ratio,  $\text{PA } R_{\text{dye}}$  (equation ( 5 )), and their respective errors for measurements made on a phantom with a single dye-filled tube. The mean error in the absolute concentrations and the concentration ratios is also provided.

Dye	Known $c_{\text{dye}}$ [ $\text{mg l}^{-1}$ ]	PA $c_{\text{dye}}$ [ $\text{mg l}^{-1}$ ]	Error in PA $c_{\text{dye}}$ [%]	Known $R_{\text{dye}}$ [%]	PA $R_{\text{dye}}$ [%]	Error in PA $R_{\text{dye}}$ [% $R_{\text{dye}}$ ]
ADS740	38.0	23.1	-39.2	57.2	42.8	-14.4
ADS780	0.0	0.0	n.a.			
ADS830	28.4	30.9	+8.8			
ADS740	19.0	22.4	+17.9	30.8	28.4	-2.4
ADS780	0.0	0.0	n.a.			
ADS830	42.6	56.4	+32.4			
ADS740	57.0	72.7	+27.5	80.1	78.0	-2.1
ADS780	0.0	0.0	n.a.			
ADS830	14.2	20.5	+44.4			
ADS740	0.0	0.0	n.a.	57.6	63.9	+6.3
ADS780	38.6	51.8	+34.2			
ADS830	28.4	29.3	+3.2			
<b>Mean</b>			<b>+16.1 ± 26.2</b>			<b>-3.1 ± 8.5</b>

**Table 1** Concentrations of near-infrared dyes (PA  $c_{\text{dye}}$ ), the ratio of the determined concentrations ( $R_{\text{dye}}$ ) and their errors determined from multiwavelength photoacoustic images detected in a phantom containing a single tube

The values for PA  $c_{\text{dye}}$  show a systematic error by overestimating the dye concentrations by 16.1% on average. However, the determined concentration ratios show generally good agreement with the known  $R_{\text{dye}}$  with a mean error of -3.1% $R_{\text{dye}}$ . As part of the model inversion, the scattering coefficient was also determined as  $10\text{mm}^{-1}$ , which compares well with the known value of  $13\text{mm}^{-1}$ .

The results of the measurements made in a phantom containing three tubes are shown in Table 2. In this case, the overestimation in the absolute dye concentrations was found to be worse (+44.8%) compared to the results from the single tube phantom. However, the agreement of PA  $R_{\text{dye}}$  with the known ratio is again reasonable.

Dye	Known $c_{\text{dye}}$ [mg l <sup>-1</sup> ]	PA $c_{\text{dye}}$ [mg l <sup>-1</sup> ]	Error in PA $c_{\text{dye}}$ [%]	Known $R_{\text{dye}}$ [%]	PA $R_{\text{dye}}$ [%]	Error in PA $R_{\text{dye}}$ [% $R_{\text{dye}}$ ]
ADS740	19.0	43.4	+128.2	57.2	42.8	+12.7
ADS780	0.0	0.0	n.a.			
ADS830	42.6	56.4	+32.5			
ADS740	38.0	48.6	+27.8	30.8	28.4	+2.9
ADS780	0.0	0.0	n.a.			
ADS830	28.4	32.3	+13.9			
ADS740	57.0	67.4	+18.3	80.1	78.0	-3.8
ADS780	0.0	0.0	n.a.			
ADS830	14.2	21.0	+47.9			
<b>Mean</b>			<b>+44.8 ± 42.6</b>			<b>+3.9 ± 8.3</b>

**Table 2** Concentrations of near-infrared dyes (PA  $c_{\text{dye}}$ ), the ratio of the determined concentrations ( $R_{\text{dye}}$ ) and their errors determined from multiwavelength photoacoustic images detected in a phantom containing three tubes.

#### 4.2. In vivo results

The HbO<sub>2</sub> and HHb concentrations, the total haemoglobin concentration and the blood sO<sub>2</sub> in three individual blood vessels determined from multiwavelength photoacoustic images are shown in Table 3. In the absence of an independent measurement, these values are best compared to reported physiological values:  $c_{\text{THb}}$  is typically  $150\text{ g l}^{-1}$ , while the venous blood sO<sub>2</sub> measured in the finger and hand has been reported to range from 76-90% $s\text{O}_2$  [11]. The photoacoustically determined values for  $c_{\text{THb}}$  show significant differences to the physiological mean, ranging from underreading for vessel 1 to significant overreading for vessel 3. Blood sO<sub>2</sub> also shows significant variations between the blood vessels but the values agree reasonably well with those reported as the physiological range. The extravascular HbO<sub>2</sub> and HHb concentrations were determined as  $0.8\text{ g l}^{-1}$  and  $0\text{ g l}^{-1}$ , respectively, which agrees with the reported physiological values of  $0.7\text{-}3.3\text{ g l}^{-1}$  [12] although the extremely high oxygenation of the extravascular haemoglobin, which is presumed to be located in the capillary bed, is perhaps questionable.

Blood vessel #	$c_{\text{HbO}_2}$ [g l <sup>-1</sup> ]	$c_{\text{HHb}}$ [g l <sup>-1</sup> ]	$c_{\text{THb}}$ [g l <sup>-1</sup> ]	Blood sO <sub>2</sub> [%]
1	103.6	24.8	128.4	80.7
2	152.8	68.2	221.0	69.1
3	228.2	22.8	251.0	90.9

**Table 3** Intravascular oxy- and deoxyhaemoglobin concentrations, the total haemoglobin concentration, and the blood sO<sub>2</sub> determined from multiwavelength photoacoustic images of individual blood vessels in the finger.

## 5. DISCUSSION

The measurements on tissue phantoms have shown that the proposed method is able to detect the presence of particular dyes with high specificity. In addition, the ratio of the dye concentrations was in good agreement with the expected values. However, the absolute concentrations showed significant errors. Although these results may at first seem contradictory, they are explained by analysing the ability of the current forward model to accurately predict both the shape and the amplitude of the measured spectra. To recover absolute concentrations, the model output has to fit to all spectra contained in the multiwavelength images simultaneously. The model must therefore accurately describe not only the shape of each spectrum but correctly scale them relative to each other. If this is not fulfilled, an error in the absolute chromophore concentrations returned by the inversion will be introduced. However, this error will be the same for all determined concentrations and therefore cancel when the dye ratio (or blood  $sO_2$ ) is calculated. The implication of this explanation is that the model accurately describes the shape of the measured photoacoustic spectra. The incorrect scaling of the predicted spectra is due to, for example, inaccuracies in the assumed location and profile of the excitation beam in the FEM, but also the inherent error in the location of the absorbing regions, which arises from manually defining their position in the FEM based on detected photoacoustic images that are themselves subject to, for example, reconstruction artefacts.

The absolute values for  $c_{HbO_2}$  and  $c_{Hb}$  showed significant deviation from the physiological norm, while the determined blood  $sO_2$  values agreed well with published data. Here, a number of additional limitations contributed to the errors. The most important limitation lies in the two-dimensional model, when in reality, the light transport and acoustic propagation occupy a 3D domain. In addition, movement artefacts are likely to have corrupted the detected spectra, which may also have affected the determined blood  $sO_2$ .

Despite these limitations, the initial results are nevertheless encouraging for future work. In order to enable the accurate quantitative measurement of chromophore concentrations, the ability of the FEM to predict the relative amplitude of detected spectra needs to be improved. In order to make the method generally applicable, the model will be configured such that the absorption coefficient (expressed in terms of chromophore concentrations) of each pixel will be variable. Finally, the model will be extended to 3D.

## 6. REFERENCES

1. K. Maslov, M. Sivaramakrishnan, H. F. Zhang, G. Stoica, and L. V. Wang, "Technical considerations in quantitative blood oxygenation measurement using photoacoustic microscopy in vivo," *PHOTONS PLUS ULTRASOUND: IMAGING AND SENSING 2006 PROGRESS IN BIOMEDICAL OPTICS AND IMAGING* **6086**, 60860R-1-60860R-11 (2006).
2. K. M. Stantz, B. Liu, M. Cao, D. Reinecke, K. Miller, and R. Kruger, "Photoacoustic spectroscopic imaging of intra-tumor heterogeneity and molecular identification," *PHOTONS PLUS ULTRASOUND: IMAGING AND SENSING 2006 PROGRESS IN BIOMEDICAL OPTICS AND IMAGING* **6086**, 608605-1-608605-11 (2006).
3. X. Wang, X. Xie, G. Ku, and L. V. Wang, "Noninvasive imaging of hemoglobin concentration and oxygenation in the rat brain using high-resolution photoacoustic imaging," *Journal of Biomedical Optics* **11**, 024015-1-024015-9 (2006).
4. J. Laufer, C. Elwell, D. Delpy, and P. Beard, "Quantitative spatially resolved measurement of tissue chromophore concentrations using photoacoustic spectroscopy: application to the measurement of blood oxygenation and haemoglobin concentration," *Physics in Medicine and Biology* **52**, 141-168 (2007).
5. R. A. Kruger, W. L. Kiser, D. R. Reinecke, G. A. Kruger, and K. D. Miller, "Thermoacoustic molecular imaging of small animals," *Molecular Imaging* **2**, 113-123 (2003).
6. X. Xie, M.-L. Li, J.-T. Oh, G. Ku, C. Wang, C. Li, S. Similache, G. F. Lungu, G. Stoica, and L. V. Wang, "Photoacoustic molecular imaging of small animals in vivo," *PHOTONS PLUS ULTRASOUND: IMAGING AND SENSING 2006 PROGRESS IN BIOMEDICAL OPTICS AND IMAGING* **6086**, 608606-1-608606-6 (2006).

7. J. Laufer, C. Elwell, D. Delpy, and P. Beard, "In vitro measurements of absolute blood oxygen saturation using pulsed near-infrared photoacoustic spectroscopy: accuracy and resolution," *Physics in Medicine and Biology* **50**, 4409-4428 (2005).
8. H. J. van Staveren, C. J. M. MOES, J. van Marle, S. A. Prahl, and M. J. C. van Gemert, "Light-scattering in Intralipid 10% in the wavelength range of 400-1100nm," *Applied Optics* **30**, 4507-4514 (1991).
9. E. Z. Zhang and P. C. Beard, "2D backward-mode photoacoustic imaging system for NIR (650-1200nm) spectroscopic biomedical applications," *PHOTONS PLUS ULTRASOUND: IMAGING AND SENSING 2006 PROGRESS IN BIOMEDICAL OPTICS AND IMAGING* **6086**, 60860H-1-60860H-7 (2006).
10. K. P. Köstli and P. C. Beard, "Two-dimensional photoacoustic imaging by use of Fourier- transform image reconstruction and a detector with an anisotropic response," *Applied Optics* **42**, 1899-1908 (2003).
11. M. Nitzan, M. A. Babchenko, and B. Khanokh, "Measurement of oxygen saturation in venous blood by dynamic near infrared spectroscopy," *Journal of Biomedical Optics* **5**, 155-162 (2000).
12. R. M. P. Doornbos, R. Lang, M. C. Aalders, F. W. Corss, and H. J. C. M. Steerenborg, "The determination of *in vivo* human tissue optical properties and absolute chromophore concentrations using spatially resolved steady-state diffuse reflectance spectroscopy," *Physics in Medicine and Biology* **44**, 967-981 (1999).